Available online at www.sciencedirect.com

ScienceDirect

Trans. Nonferrous Met. Soc. China 34(2024) 2589−2604

Transactions of
Nonferrous Metals
Society of China

www.tnmsc.cn

Damage characteristics of Cu−Cr−Zr alloy rail of electromagnetic railgun after simulated launch

Ke-chang SHEN[1], Qing-tao GONG[1], Zhong-yu SUN[1], Hong-tu SUN[1], Bin-jie MA[1], Wei-min WANG[2]

1. Ulsan Ship and Ocean College, Ludong University, Yantai 264025, China;
2. Key Laboratory for Liquid-Solid Structural Evolution and Processing of Materials, Ministry of Education,
School of Materials Science and Engineering, Shandong University, Jinan 250061, China

Received 9 October 2023; accepted 24 April 2024

Abstract: The damage characteristics of different speed sections of Cu−Cr−Zr alloy rail after simulated launch were studied. The microstructure, morphologies and properties of samples were investigated by using XRD, XPS, EBSD, SEM, hardness test, electrochemical test and DSC techniques. It was found that deposition layers were formed on the surfaces of the simulated launch samples. The thickness and surface roughness of these deposition layers increased with increasing the heat effect, suggesting a launch speed dependent damage degree of the arc ablation. The hardness variation of samples is attributed to the effects of the deposition layer and deformation hardening. The surface deposition layer affects corrosion resistance and crystalline characteristics, leading to changes in subsequent service performances. Additionally, the surface texture and plastic deformation ability of the samples are related to the recrystallization degree and deformation grain amount.

Key words: Cu−Cr−Zr alloy; electromagnetic railgun; arc ablation; microstructure; performance

---

1 Introduction

The electromagnetic railgun is a new concept of the advanced kinetic energy weapon with a fast projectile launch speed, a long range, a high power and a strong controllability. It breaks through the speed limitation of traditional cannons and has a good development potential in military applications such as air defense and long range attack [1]. During the launch process, the rail and armature are subjected to harsh operating conditions such as high current, high temperature, strong magnetic field and high impact, resulting in the surface damages like arc ablation, gouging, softening and friction wearing [2]. Consequently, these damages can decline the service life of rail material. In fact, the performance of rail material is the key to determining the engineering application of electromagnetic railgun, therefore it is necessary to have good strength and high ablation resistance. The damage analysis and performance improvement of rail material have become a research hotspot for the electromagnetic railgun.

As a typical precipitation strengthening alloy, Cu−Cr−Zr alloy has a combination of superior properties like strength, electrical conductivity, thermal stability and corrosion resistance [3]. Hence, it has important applications in various industrial and military fields, such as high-speed railway contact wires, electrical contact components, integrated circuit lead-frame materials, heat exchangers in the international thermonuclear experimental reactors, spot welding electrodes and

---

Corresponding author: Qing-tao GONG, Tel: +86-15653500211, E-mail: gongqt@ldu.edu.cn;
Wei-min WANG, Tel: +86-13698615118, E-mail: weiminw@sdu.edu.cn

DOI: 10.1016/S1003-6326(24)66562-3

passive satellites [4,5]. Especially, it is an important rail material of the electromagnetic railgun.

The Cu−Cr−Zr alloy contains trace amount of Cr and Zr. The equilibrium solubility of Cr and Zr in Cu matrix is very low (only ~0.03 wt.% Cr and ~0.01 wt.% Zr) at room temperature, and the Cu−Cr−Zr alloy is mainly composed of Cu-based solid solutions, Cu_xZr and Cr [6,7]. The solution treatment, plastic deformation and aging can usually be used to optimize the comprehensive performance of Cu−Cr−Zr alloy [7,8]. Since Cu−Cr−Zr alloy has important application in the electromagnetic railgun rail, its damage characteristic during launch process is crucial. There are some investigations about the arc ablation of Cu alloys using simulated arc ablation experiments. LI et al [9] found that molten pits formed on the $CuZr/Zn_2SnO_4$ surface, and the formation of Zr and Cu oxides can prevent the expansion of molten pits. ZHOU et al [10] reported that based on the comprehensive effect of different strengthening mechanisms, the ablation resistance of Cu−Cr−Zr alloy was significantly improved. However, there is little research on the damage characteristic of rail material after launch. The lack of understanding on the surface damage and performance change of Cu−Cr−Zr alloy under high-temperature thermal impact limits the improvement of service life and safety. Hence, it is necessary to investigate the surface morphology and performance of the electromagnetic railgun rail after launch.

In this work, the microstructure, surface morphology, mechanical properties, corrosion resistance, high-temperature performance, and texture of different launch speed sections of Cu−Cr−Zr alloy rails after simulated launch were investigated. It is hoped that this work can provide valuable references for understanding the damage characteristics, improving the rail performance and promoting the development of electromagnetic railgun.

2 Experimental

Figure 1 shows the schematic diagram of the electromagnetic railgun. It consists of two parallel conductor rails on which the armature makes electrical contact. When the current flows in the rails, a magnetic field is generated. The interaction between the magnetic field and the current can generate the Lorentz force, which drives the armature to move rapidly with the projectile.

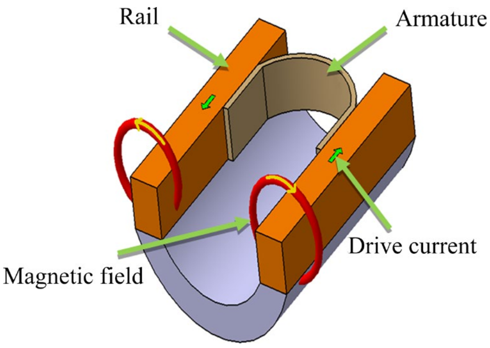

Fig. 1 Schematic diagram of electromagnetic railgun

The tested materials were cut from the Cu−Cr−Zr alloy rail surfaces which contacted with armature before and after simulated launch experiment (launch times: ≥10) using DK7735 numerical control wire cutting machine. The composition of original Cu−Cr−Zr alloy is shown in Table 1, and the armature material is 7075 Al alloy. The rails were mainly subjected to heat caused by the current and impact during the launch process. Based on the armature running speed (i.e. launch speed), the rail can be divided into low speed (about 500 m/s), medium speed (about 1000 m/s) and high speed (about 2000 m/s) sections. In fact, a lower launch speed means a longer contact time between the rail and armature, leading to a higher heat subjected by rail sample. The low speed section sample (suffered to high heat effect), medium speed section sample (suffered to medium heat effect), high speed section sample (suffered to low heat effect) and original sample (without heat effect) are respectively named as J_H, J_M, J_L and J_O.

Table 1 Composition of original Cu−Cr−Zr sample (wt.%)

Cu	Cr	Zr
98.9	1.0	0.1

The phase compositions of samples were investigated by X-ray diffraction (XRD, XD−3) with a Cu target (Cu K_α radiation, λ=0.154056 nm). The surface morphologies and the micro area compositions of samples were observed using field emission scanning electron microscopy (SEM, JSM−7610F) equipped with energy dispersive spectrometry (EDS). The element valence states on the sample surfaces were investigated by X-ray photoelectron spectroscopy (XPS, Axis Supra) with Al K_α radiation. The binding energies of tested elements were calibrated by carbon contamination with a C 1s peak (284.8 eV).

The hardness of sample was tested using a Brinell hardness tester (HBS−3000). The indenter diameter was 5.0 mm, the applied load was 2450 N and the holding time was 15 s. Each sample was tested 8 times and the average hardness value was taken.

The electrochemical measurements were conducted using an advanced electrochemical workstation (CHI 660E, Shanghai Chenhua Instrument Co., Ltd., China) with a typical three-electrode system (working electrode, counter electrode and reference electrode). The tested solution is 3.5 wt.% NaCl solution, counter electrode is Pt foil and reference electrode is $Hg|Hg_2Cl_2$ (SCE). The nitrogen was introduced into the solution to remove dissolved oxygen, and then the open circuit potentials were tested for 20 min. When the open circuit potentials were stable, potentiodynamic polarization curves were scanned with a scan rate of 1 mV/s. Electrochemical impedance spectroscopy (EIS) tests (frequency: 0.01−100000 Hz and potential amplitude: 0.01 V) were also conducted, and the data were fitted by ZsimDemo software.

The thermal properties of samples were investigated using differential scanning calorimetry (DSC, Netzsch DSC404) under a flow of high purity argon. During the measurement, the samples were heated from 40 to 1150 °C, and then they were cooled to 300 °C. Both heating rate and cooling rate are 10 °C/min.

In order to characterize the structural change and plastic deformation of the sample, the electron backscattered diffraction (EBSD, equipped with the Hitachi S−3400N SEM) tests were conducted. Before the test, the samples were ion-etched (Voltage: 6 kV; incident angle: 8°; time: 45 min). The orientation map, pole figure, misorientation angle distribution, grain boundary distribution and Schmid factor (SF) were obtained using the software of HKL Channel 5.

3 Results and discussion

3.1 Surface structure, morphology and hardness

Figure 2 shows the XRD patterns of Cu−Cr−Zr samples. There are more diffraction peaks for the samples after simulated launch (J_H, J_M and J_L) than those for the original sample (J_O), indicating the significant changes of surface microstructure

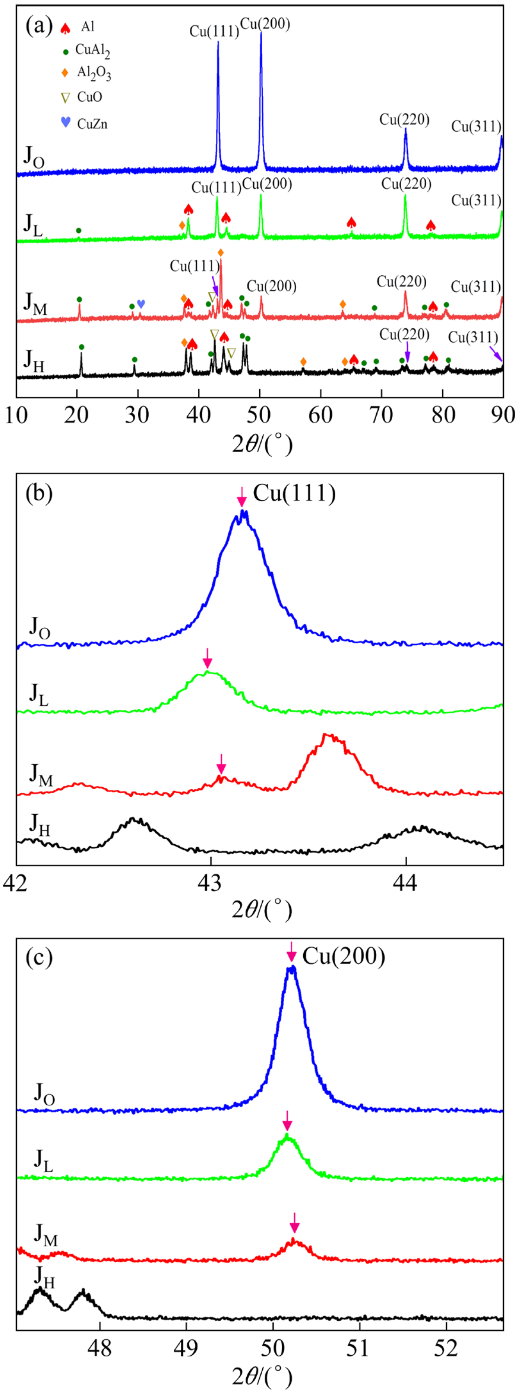

Fig. 2 XRD patterns of Cu−Cr−Zr samples (a) and enlarged parts for Cu(111) (b) and Cu(200) (c) diffraction peaks

caused by heat and impact. During the launch process, strong contact current generated an arc between the rail and armature, resulting in severe arc ablation at the interface between them [11,12]. Due to the arc ablation, the Al armature melted and subsequently deposited onto the rail surfaces [2,13]. Hence, the number of diffraction peaks increases with the increase of heat (i.e. decrease of launch speed). The (111), (200), (220) and (311) peaks of fcc Cu can be identified for samples [14]. It can also be seen clearly that the intensities of Cu diffraction peaks decrease with the increase of heat, suggesting the change of Cu content and texture. The diffraction peaks of Al, $CuAl_2$, Al_2O_3, CuO and CuZn are identified for J_H, J_M and J_L samples, indicating the formation of some oxides and compounds (Fig. 2(a)). It is thought that there are deposition layers on the simulated launch sample surfaces caused by arc ablation, which will be further proven in subsequent discussion.

However, due to the solid solubility and tiny content, there is no diffraction peak for Cr and Zr elements [15]. According to the position variations of Cu(111) and Cu(200) peaks, it can be found that the peak position (2θ) changes with increasing the heat (Figs. 2(b) and (c)). Due to the thickest surface deposition layer on the J_H sample, which will be further proven in subsequent discussion, Cu(111) and Cu(200) peaks are not identified in its XRD pattern. Based on extended Bragg equation, the change of θ indicates the change of lattice constant a_0 [16]. Hence, it is thought that the solubility of alloy elements in Cu changed during the launch process, thus resulting in the lattice distortion [15,17].

Figure 3 shows the SEM images of sample surfaces together with their pictures. It can be seen from their pictures that J_H, J_M and J_L samples have gray surfaces, while J_O sample has original color. Here, J_H surface is the roughest among four samples, suggesting that it experiences the most serious ablation and that the ablation degree of the rail increases with increasing the heat or with decreasing the launch speed. There are products with a certain thickness on the J_H, J_M and J_L sample surfaces, indicating the formation of deposition layer after simulated launch. In addition, there is a spalling phenomenon occurring on the deposition layer. These surface morphologies can be ascribed to the combined action of arc ablation, melting and friction caused by the heat and impact.

According to EDS analysis results of sample surfaces, which are shown in Figs. S1 and S2 in Supplementary Materials (SM), there are Cu, Cr,

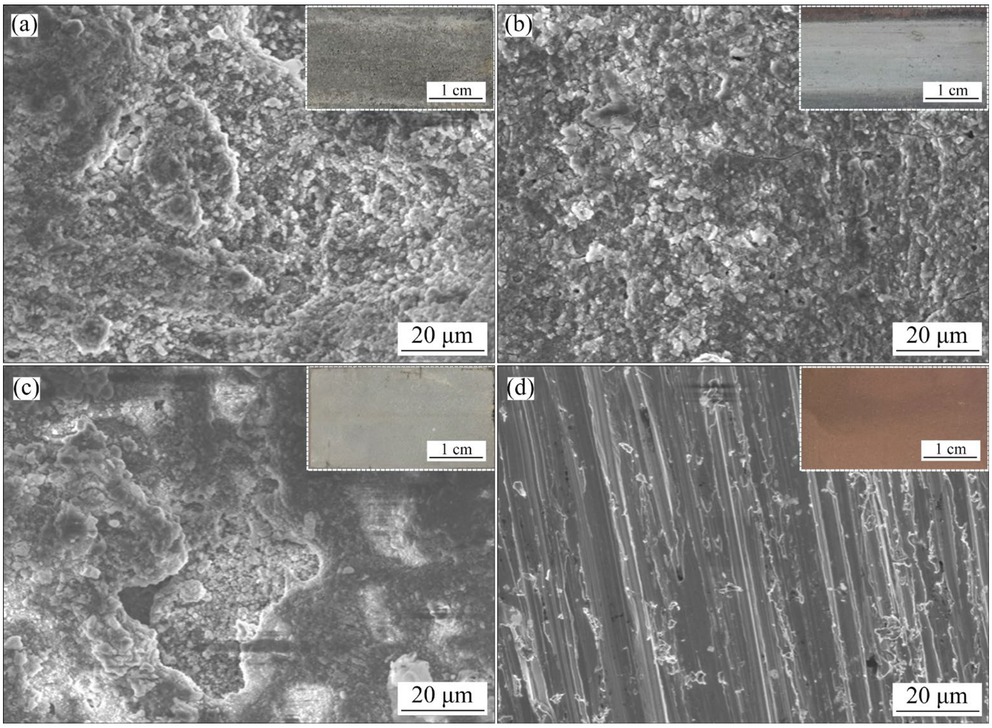

Fig. 3 Morphologies of Cu−Cr−Zr sample surfaces (The insets are the corresponding surface pictures): (a) J_H; (b) J_M; (c) J_L; (d) J_O

Zr, Al, Zn, Mg and O elements on the J_H, J_M and J_L sample surfaces, and only Cu, Cr and Zr elements are detected on the J_O sample surface, being consistent with the XRD results. Al content of deposition layer is very high, and O content decreases with the decrease of heat, which may be related to the variation of deposition layer thickness. Based on EDS and XRD results, the deposition layer should be mainly composed of oxides and compounds of Cu, Al, Zn and Mg elements.

The cross-section morphologies of simulated launch samples were observed, as shown in Fig. S3 in SM. The surface deposition layers of samples are relatively rough. The deposition layer thickness of J_H, J_M and J_L samples is approximately 166, 32 and 24 μm, respectively, showing a decreasing tendency with the decrease in heat. There are some holes in the deposition layers, possibly being related to two factors: (1) difference in expansion coefficients and coordination mismatch of various components in deposition layers; (2) liquid Al formed at the interface between the rail and armature due to the high heat, and then the water vapor in air was dissolved in the liquid Al to form H_2 ($2Al+3H_2O \rightarrow Al_2O_3+3H_2\uparrow$), and finally H_2 escaped from liquid Al which had been deposited on the rail surface. The EDS results of cross-section indicate that the Al, Zn, Mg and O contents of deposition layer are higher than those of the matrix, which is consistent with the EDS results of sample surfaces (Figs. S1 and S3 in SM). However, the elements of deposition layer can diffuse into the matrix. As a consequence, small amount of Al and Zn elements can be detected in the matrix close to deposition layer (Fig. S3(d) in SM). Additionally, Cu and Cr contents of deposition layers are lower than those of the matrix, whereas the Zr content shows an opposite change, suggesting that Zr element is easily enriched in deposition layer.

In order to further investigate the characteristic of deposition layer, the EIS measurement was conducted. Figure 4 shows the Nyquist plots and Bode plots of Cu−Cr−Zr samples in 3.5 wt.% NaCl solution. It can be found that the Nyquist plots for J_H, J_M and J_L samples are composed of single capacitive loop, indicating that the corrosion processes are controlled by electrochemical reactions. The Nyquist plot for J_O sample is composed of a capacitive loop and a Warburg impedance, which indicates a corrosion process controlled by diffusion [18]. In the medium frequency and high ranges of the Bode plots, the phase angles are close to 75°, and there is a linear relationship between $|Z|$ and frequency. Hence, it can be inferred that the samples exhibit certain capacitance characteristics within these frequency ranges, indicating the presence of sparse and porous oxidation films on the sample surfaces [19,20]. However, there are deposition layer, oxidation film and holes on the simulated launch sample surfaces, leading to a complex electrode system. An equivalent circuit model of $R(C(R(Q(R(LR)(CR)))))$ for simulated launch sample is shown in the inset of Fig. 4(a), and the corresponding circuit element parameters are listed in Table 2, where R represents the resistance element (R_s: solution resistance; R_{dl}: double electric layer resistance; R_f: surface oxidation film resistance; R_L: inductive resistance; R_C: capacitance resistance), C represents the capacitance element (C_{dl}: double electric layer capacitance; C_f: film capacitance), L_f represents the film inductance, and Q is the constant phase element (CPE). The impedance of CPE (Z_{CPE}) can be expressed by the following equation [21]:

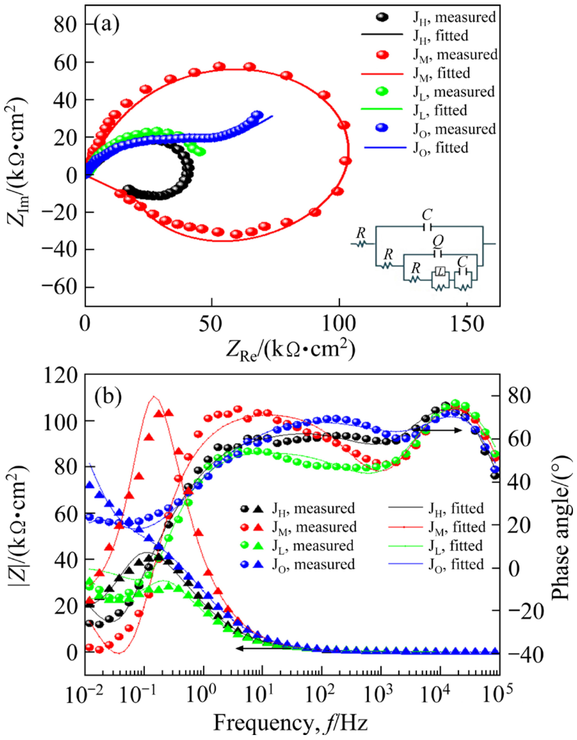

Fig. 4 Nyquist (a) and Bode plots (b) of Cu−Cr−Zr samples in 3.5 wt.% NaCl solution (The inset in (a) is fitted equivalent circuit of electrochemical impedance spectroscopy (EIS) for simulated launch samples)

$$Z_{\mathrm{CPE}}=\frac{1}{Y_0}(\mathrm{J}\omega)^{-m} \tag{1}$$

where Y_0 is the admittance, J is the imaginary number ($\mathrm{J}^2=-1$), ω is the angular frequency, and m with value between 0 and 1 represents the phase shift. When m value approaches 1, Q suggests a pure capacitance; while m=0, it represents the pure resistance behavior. As shown in Fig. S4 in SM, the sum of R_{f} and R_{L} are considered as equivalent resistance. It can be found that the equivalent resistance values of $\mathrm{J_M}$ and $\mathrm{J_L}$ are higher than that of $\mathrm{J_O}$ sample, which is due to the formation of deposition layer on the simulated launch sample surfaces. However, the $\mathrm{J_H}$ sample, with the thickest deposition layer, has the lowest equivalent resistance. This is because the deposition layer cracked due to the large difference in expansion coefficients and coordination mismatch of various components under high heat.

To study the surface element valence states, an XPS measurement was conducted. The wide scan XPS spectra of Cu−Cr−Zr samples are shown in Fig. 5. The peak intensities for O 1s in the simulated launch samples are higher than those in the original sample, while the peak intensities for Cu 2p show the opposite trend, indicating the formation of oxides on the surfaces of $\mathrm{J_H}$, $\mathrm{J_M}$ and $\mathrm{J_L}$ samples. The detailed XPS spectra for Cu 2p are presented in Fig. 6. The binding energies of Cu $2\mathrm{p}_{3/2}$ and Cu $2\mathrm{p}_{1/2}$ for $\mathrm{J_O}$ sample are respectively 932.50 and 952.32 eV, which could be referred to Cu^0 [22,23]. The satellite peaks (marked as shake-up around 943 and 963 eV) are observed for $\mathrm{J_H}$, $\mathrm{J_M}$ and $\mathrm{J_L}$ samples [24]. Additionally, the binding

Table 2 Parameters of elements in equivalent circuit to fit EIS for simulated launch samples (χ^2<0.004)

Sample	R_{s}/ (Ω·cm²)	C_{dl}/ (F·cm⁻²)	R_{dl}/ (Ω·cm²)	Q/ (F·cm⁻²)	m	R_{f}/ (Ω·cm²)	L_{f}/ (H·cm²)	R_{L}/ (Ω·cm²)	C_{f}/ (F·cm⁻²)	R_{C}/ (Ω·cm²)
$\mathrm{J_H}$	4.6	3.8×10^{-7}	199	9.0×10^{-6}	0.71	0.01	9.3×10^{4}	3.5×10^{4}	2.1×10^{-6}	1.7×10^{4}
$\mathrm{J_M}$	6.1	2.2×10^{-7}	295	4.5×10^{-6}	0.82	0.02	1.6×10^{5}	1.1×10^{5}	8.9×10^{-7}	2.4×10^{4}
$\mathrm{J_L}$	6.6	1.8×10^{-7}	316	1.5×10^{-6}	0.64	2.2×10^{4}	1.7×10^{4}	4.3×10^{4}	3.4×10^{-4}	85

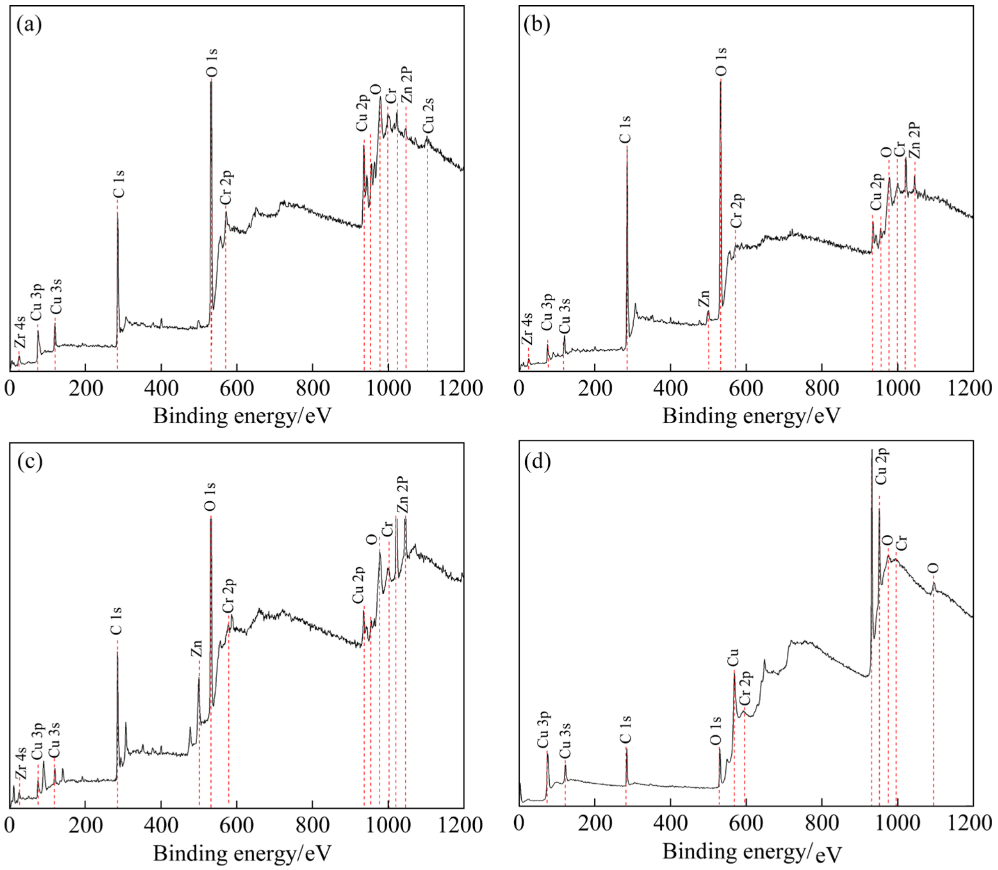

Fig. 5 Wide scan XPS spectra for Cu−Cr−Zr samples: (a) $\mathrm{J_H}$; (b) $\mathrm{J_M}$; (c) $\mathrm{J_L}$; (d) $\mathrm{J_O}$

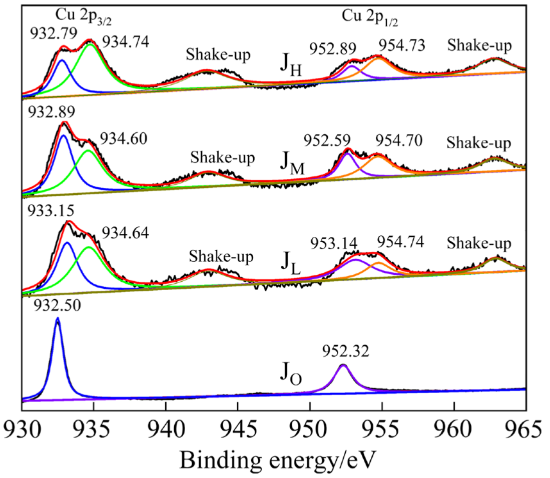

Fig. 6 Detailed XPS spectra for Cu 2p of Cu−Cr−Zr samples

energies of Cu 2p for $\mathrm{J_H}$, $\mathrm{J_M}$ and $\mathrm{J_L}$ samples are higher than those for $\mathrm{J_O}$ sample, indicating a higher oxidized state of the simulated launch sample surface. Based on the deconvolution of XPS spectra, the binding energies of Cu 2p for simulated launch samples can be attributed as coexistence of $\mathrm{Cu^0}$ (932.79−933.15 eV for Cu $2p_{3/2}$ and 952.59−953.14 eV for Cu $2p_{1/2}$) and $\mathrm{Cu^{2+}}$ (934.60−934.74 eV for Cu $2p_{3/2}$ and 954.70−954.74 eV for Cu $2p_{1/2}$) [24,25]. Thus, the XPS data also indicate the formation of oxide deposition layers on the sample surfaces after simulated launch.

Figure 7 shows the Brinell hardness of the Cu−Cr−Zr samples. The hardness values of simulated launch samples are evidently higher than that of original sample ($\mathrm{J_H}$: HBW 128.3, $\mathrm{J_M}$: HBW 110.5, $\mathrm{J_L}$: HBW 116.9, and $\mathrm{J_O}$: HBW 109.4), indicating that the formation of deposition layer enhances the surface hardness. For simulated launch samples, the hardness values from high to low can be ranked as: $\mathrm{J_H}>\mathrm{J_L}>\mathrm{J_M}$. It is thought that the hardness of sample is related to the surface deposition layer and deformation hardening caused by the heat and impact. In addition, more alloy elements in the deposition layer may lead to a better solid solution strengthening effect. Hence, the $\mathrm{J_H}$ sample, which has the thickest deposition layer, exhibits the highest hardness value. However, there is minor difference in the deposition layer thickness for $\mathrm{J_M}$ and $\mathrm{J_L}$ samples (Fig. S3 in SM). But $\mathrm{J_L}$ sample suffered a larger impact due to a higher launch speed. So $\mathrm{J_L}$ sample actually has a higher deformation hardening effect than $\mathrm{J_M}$ sample. As shown in Fig. 8, with the decrease of hardness, the shape of Brinell hardness indentation becomes much clearer. Moreover, the size of indentation for $\mathrm{J_H}$ sample is the smallest, while that for $\mathrm{J_O}$ sample is the largest, which is consistent with their hardness values.

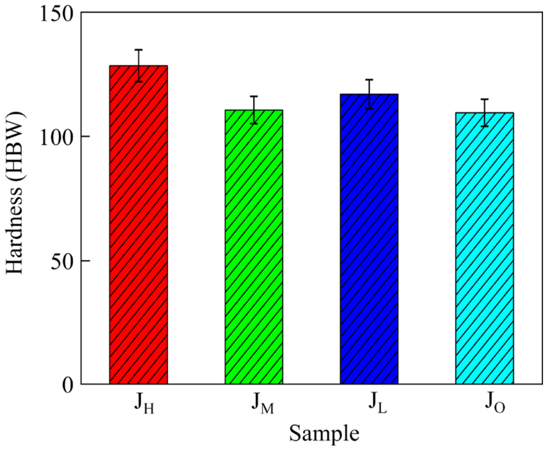

Fig. 7 Brinell hardness of Cu−Cr−Zr samples

3.2 Electrochemical corrosion resistance

Since the sample surfaces will be oxidized during launch process, the oxidation resistance of surface deposition layer can affect the subsequent launch. The electrochemical corrosion can also lead to the surface oxidation, which may be helpful for further understanding the oxidation resistance behavior of Cu−Cr−Zr samples. It is expected that the electrochemical experiment results will help to understand the surface structure and the effect of deposition layer. Additionally, it can also provide some references for the corrosion resistance of rail materials in marine or humid environments.

The open circuit potential (φ_{ocp}) curves are shown in Fig. S5 in SM. The φ_{ocp} of $\mathrm{J_O}$ sample is apparently higher than that of $\mathrm{J_H}$, $\mathrm{J_M}$ and $\mathrm{J_L}$ samples ($\mathrm{J_H}$: −0.58 V; $\mathrm{J_M}$: −0.60 V; $\mathrm{J_L}$: −0.72 V; $\mathrm{J_O}$: −0.22 V). Figure 9 shows the potentiodynamic polarization curves for samples in 3.5 wt.% NaCl solution with a scan rate of 1 mV/s. There is an anodic current density peak (J_{peak} at −0.019 V (vs SCE)) on the curve of J_{O} sample, and J_{O} sample has a more stable passivation range compared with $\mathrm{J_H}$, $\mathrm{J_M}$ and $\mathrm{J_L}$ samples. Based on references [26,27], the J_{peak} is corresponding to the oxidation of Cu in the solution containing $\mathrm{Cl^-}$. Due to the formation of dense passive film on $\mathrm{J_O}$ sample, a longer passivation range appeared after J_{peak}. According to Fig. S6 in SM, the corrosion potential (φ_{corr}) and pitting

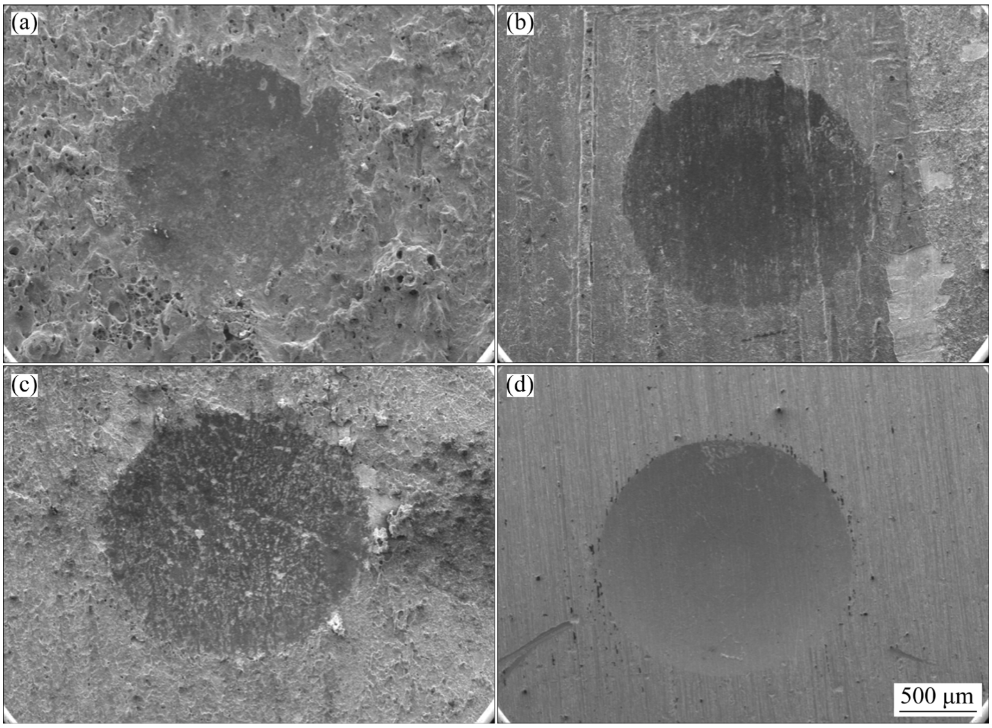

Fig. 8 SEM images of Brinell hardness indentation for Cu−Cr−Zr samples: (a) J_H; (b) J_M; (c) J_L; (d) J_O

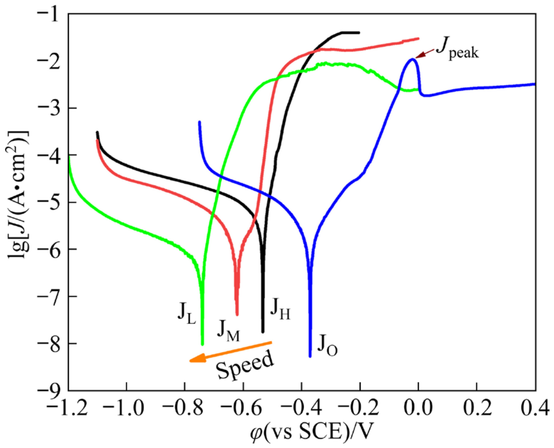

Fig. 9 Potentiodynamic polarization curves for Cu−Cr−Zr samples in 3.5 wt.% NaCl solution at scan rate of 1 mV/s

potential (φ_{pit}) of J_O sample are the highest, and their variation trends are the same as φ_{ocp}. Due to the presence of surface deposition layer, the exposed Cu content of simulated launch sample is lower than that of the J_O sample. Moreover, the deposition layer is mainly composed of oxides and compounds. Therefore, there is no apparent anodic current density peak on the polarization curve of the simulated launch sample. However, the simulated launch sample surface is much rougher than the original sample surface, and the electrode potential of alloy elements in the deposition layer is lower than that of Cu. Hence, the φ_{corr} of the J_H, J_M and J_L samples is lower than that of the J_O sample.

It is not that the thicker the deposition layer, the worse the corrosion resistance. The J_H sample has the highest φ_{corr} among the simulated launch samples. It is thought that the thickness and chemical composition of deposition layer can both affect the corrosion resistance. Firstly, a thicker deposition layer acts as a better protective layer, leading to the increase of φ_{corr}. Secondly, as the potential increases, the J_H, J_M and J_L sample surfaces can form passive films which are beneficial to improving the corrosion resistance [28]. In fact, the elements such as Cu, Cr, Zr, Al and Zn can fully diffuse between the matrix and deposition layer under a higher heat effect. Mixed passive films can then form on the surfaces of the simulated launch samples. For instance, Cr can form a dense passive film [28,29]. Hence, the J_H sample with the thickest deposition layer can form the densest passive film than the J_M and J_L samples. As the heat for the simulated launch sample increases (i.e., the thickness of the deposition layer increases), the φ_{corr}, φ_{ocp} and φ_{pit} increase. Therefore, the subsequent corrosion resistance of the low speed section of the rail (corresponding to J_H) is superior to that of the medium and high speed sections (corresponding to J_M and J_L samples), indicating variations in the service performance of different speed sections. It is essential to implement distinct treatments for various speed sections of the rail in order to achieve improved launch reliability.

Figure 10 illustrates the SEM images of Cu−Cr−Zr sample surfaces after potentiodynamic polarization test. The sample surfaces are much rougher than those before polarization test, and there is a more obvious spalling phenomenon for the deposition layer. In particular, the morphology of the J_O sample after the polarization test bears some resemblance to that of the simulated launch sample before the polarization test. This reflects similarities in the surface morphologies resulting from electrochemical oxidation and ablation oxidation, respectively (Figs. 3 and 10). As shown in Fig. S1 in SM, the main metallic elements in the deposition layers are Al and Cu which are susceptible to Cl^- [27,30]. However, Cl^- can be adsorbed by metals, leading to the formation of soluble chlorides, which in turn initiates pitting corrosion and disrupts the passive film [20]. Accordingly, it can be found that there are some pits on the sample surfaces after polarization test. The J_L sample exhibits more pits than the other samples, also indicating that the corrosion resistance of the high speed section of the rail is inferior to that of the other sections.

According to the EDS results after the polarization test (as shown in Fig. S7 in SM), with the decrease of heat, the contents of Al and O for simulated launch samples decrease, while the contents of Cu and Cl increase. As mentioned above, Cl^- can destroy the passive film, thus leading to the pitting corrosion. The thinner the deposition layer is, the more susceptible the passive film on the deposition layer is to corrosion, resulting in more exposure of the matrix. Consequently, the Cu content of J_L sample after polarization test is the highest.

3.3 High temperature properties

The heating and cooling processes of DSC experiments can partially reflect the high-temperature characteristics of the rail during the launch process. The DSC curves of Cu−Cr−Zr alloys are shown in Fig. 11. In the low temperature range (40−900 °C) of the heating process, the DSC curves do not exhibit any endothermic peak (Fig. 11(a)). There are tiny weak peaks P_1 (about 973 °C) and P_2 (about 1029 °C) in the high temperature range (900−1150 °C) of the heating process (Fig. 11(b)). Based on Ref. [31], the peaks at 972.45 °C and 1058.35 °C of the DSC curves of

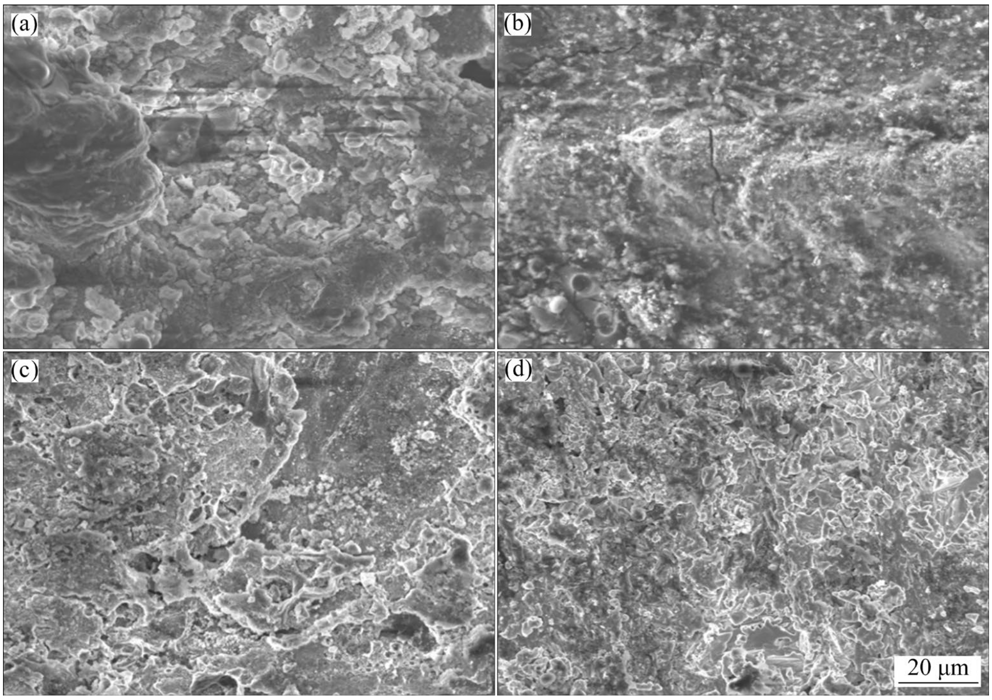

Fig. 10 Morphologies of Cu−Cr−Zr sample surfaces after potentiodynamic polarization test in 3.5 wt.% NaCl solution: (a) J_H; (b) J_M; (c) J_L; (d) J_O

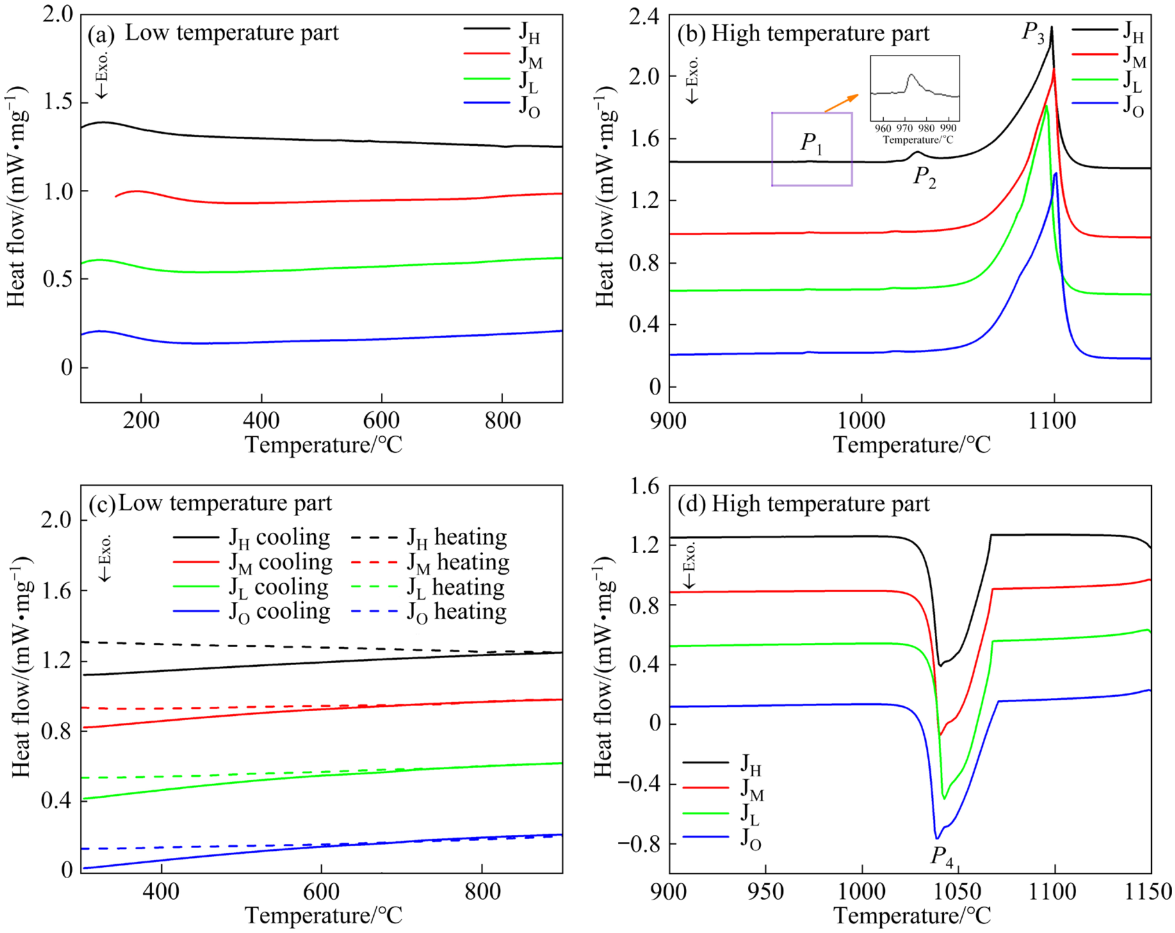

Fig. 11 DSC curves showing heating (a, b) and cooling (c, d) processes of Cu−Cr−Zr samples at heating and cooling rates of 10 °C/min

Cu−Cr−Zr alloys are attributed to invariant phase transformation reaction. At about 1100 °C, there is a strong endothermic peak P_3 corresponding to the partial melting process of Cu-based solid solution. However, even at higher temperature, certain phases with a higher melting point, such as Cr, which have low solubility in Cu, remain unmelted. Due to the presence of Al with low melting point in the deposition layer, the initial melting temperature of the J_H, J_M and J_L samples is lower than that of the J_O sample (Fig. 11(b)).

There is also no peak in the low temperature range (900−300 °C) in the cooling process (Fig. 11(c)). While there is a strong exothermic peak P_4 (around about 1040 °C) in the high temperature range (1150−900 °C) of the cooling process, being ascribed to the formation of Cu-based solid solution (Fig. 11(d)). Within the solidification temperature range, the exothermic curve initially shows a gradual decline, followed by a rapid rebound in the later stage of solidification, demonstrating the characteristics of the primary crystallization, including nucleation, growth and collision.

Furthermore, the initial crystallization temperature from high to low can be ranked as follows: $J_O>J_L>J_M>J_H$, indicating that the thicker the deposition layer is, the later the crystallization occurs, leading to a greater undercooling degree. The crystallization temperature range was calculated based on the difference between the initial crystallization temperature and the crystallization completion temperature, which is shown in Fig. S8 in SM. It is known that the crystallization temperature range is related with the composition differences of samples. A thicker deposition layer means that the sample has more low melting point elements. Therefore, the crystallization temperature ranges of the J_H, J_M and J_L samples are lower than that of the J_O sample, indicating distinct crystalline characteristics during the launch process. However, the crystallization temperature ranges of the J_H, J_M and J_L samples are relatively close, showing the slight differences among the simulated launch samples.

In summary, the deposition layers on the sample surfaces affect the variations in nucleation and growth during the launch process, thereby resulting in different surface performances.

3.4 Texture changes and plastic deformation abilities

Due to the rough surfaces of the deposition layers, it is not easy to conduct the EBSD measurement. However, the matrix surface adjacent to the deposition layer can be considered as a heat affected zone (HAZ). Therefore, the EBSD measurements for the original sample (J_O) and the HAZ of J_H and J_L samples (HAZ_{J_H} and HAZ_{J_L}) were conducted to analyze the changes of structure and properties.

As shown in Fig. 12, there are recrystallized, substructured and deformed grains in the samples. The decreasing proportion of recrystallized grain can be ranked as: HAZ_{J_H}>HAZ_{J_L}>J_O, while the fraction of deformed grain for HAZ_{J_H} is the lowest, indicating that a higher heat effect leads to a higher recrystallization degree. There are a greater number of deformed grains in HAZ_{J_L} compared to those in J_O, which can be attributed to the impact effect on J_L sample during the simulated launch process.

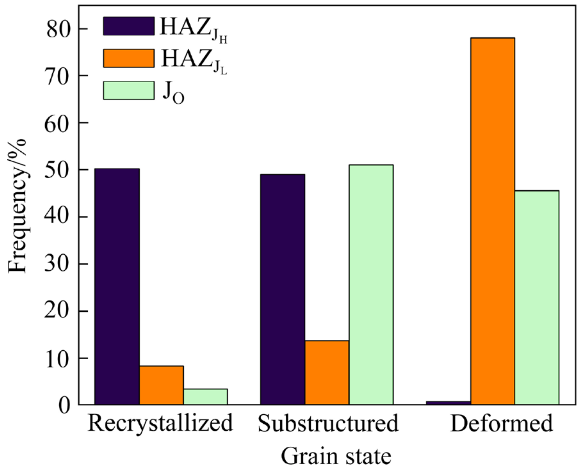

Fig. 12 Distribution of recrystallized, substructured and deformed grains of Cu−Cr−Zr samples

Figure 13 shows the orientation maps and pole figures of samples. The RD and TD refer to the rolling direction and transverse direction, respectively. It can be found that the grain size of J_O sample is larger than that of HAZ_{J_H} and HAZ_{J_L}, also indicating the occurrence of recrystallization for simulated launch samples (Figs. 13(a−c)). In fact, the heat effect on the J_H sample lasted longer, leading to a higher proportion of recrystallized grains. Based on the pole figures, the poles for HAZ_{J_H} are relatively scattered, while the pole densities for HAZ_{J_L} and J_O are much denser (Figs. 13(d−f)). The HAZ_{J_L} exhibits a ⟨110⟩ preferred orientation deviating approximately 30° from the RD and a ⟨111⟩ preferred orientation parallel to the RD. It is believed that as the heat increases, the recrystallization degree also increases, resulting in a more random grain orientation for HAZ_{J_H} [32]. In other words, the texture of the samples is influenced by the level of heat.

The misorientation angle distribution is shown in Fig. 14. The correlated and uncorrelated misorientation angles were respectively calculated from neighboring points and random points. The random misorientation distribution was deduced from a completely random texture. The difference between uncorrelated misorientation and random misorientation in HAZ_{J_L} is the most pronounced, aligning with the findings from the pole figure analysis. Furthermore, the frequency of the misorientation angle at 60° for HAZ_{J_H} is relatively high, corresponding to the (111) twin plane of fcc metal [33]. Therefore, under a longer heat influence, annealing twins appeared in HAZ_{J_H}.

The fractions of low angle grain boundary (LAGB, <5°), medium angle grain boundary (MAGB, 5°−15°) and high angle grain boundary (HAGB, >15°) calculated from the correlated misorientation are shown in Table 3. The fraction of HAGB is higher than that of LAGB for HAZ_{J_H}, which is consistent with the appearance of twin. In addition, the decreasing fraction of LAGB can be ranked as: J_O>HAZ_{J_L}>HAZ_{J_H}. Figure S9 illustrates the grain boundary distribution of samples, where the black lines denote HAGB and the green lines represent LAGB. The fraction change of LAGB aligns with the data presented in Table 3. Since LAGB is mainly composed of a series of dislocations, a decrease in the amount of dislocations can be inferred during the recrystallization process [34]. However, a high fraction of LAGB sometimes can suggest a strong texture, aligning with the observations from the pole figures [35,36].

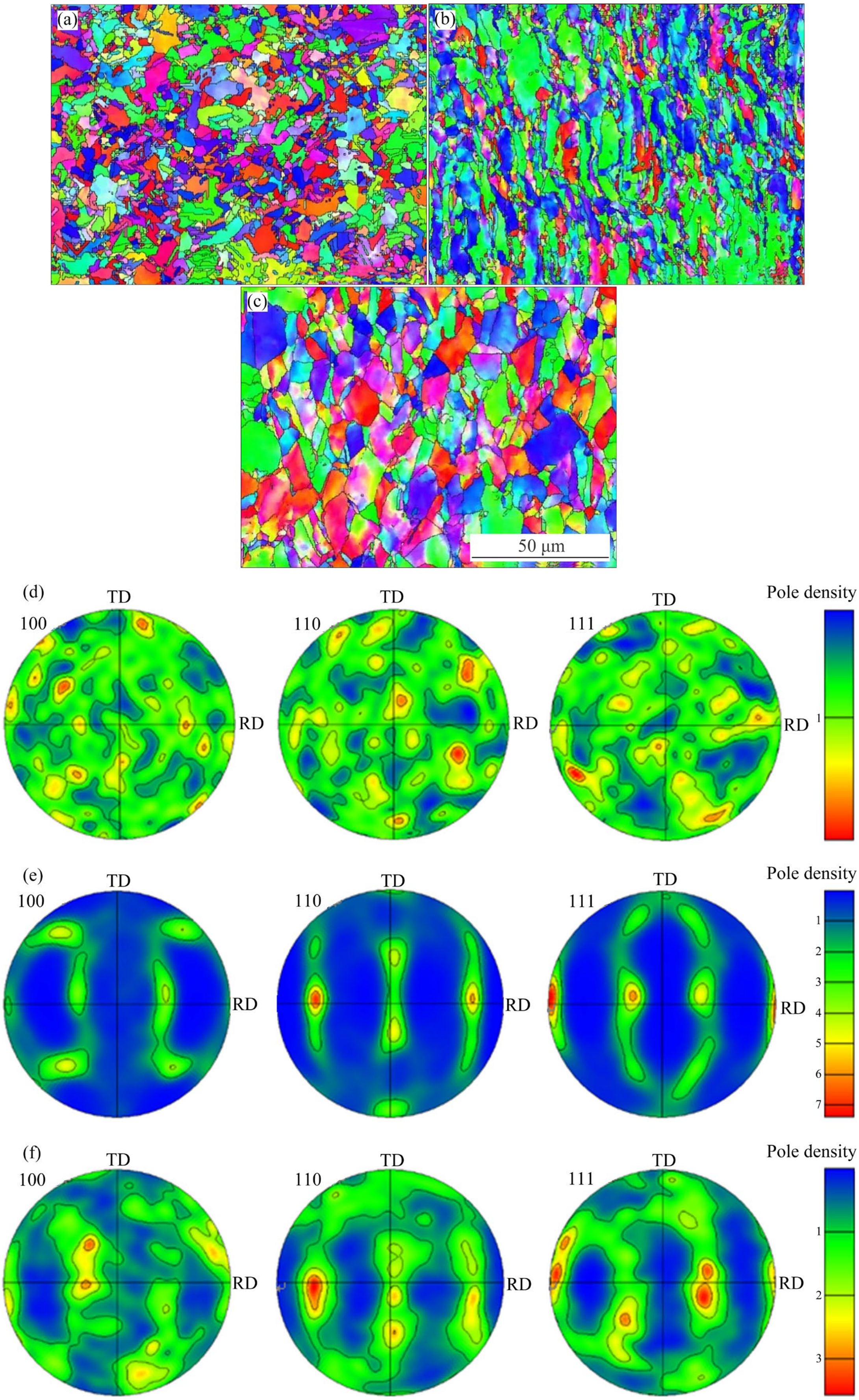

Fig. 13 Orientation maps (a−c) and pole figures (d−f) of HAZ$_{J_H}$ (a, d), HAZ$_{J_L}$ (b, e) and J$_O$ (c, f) samples

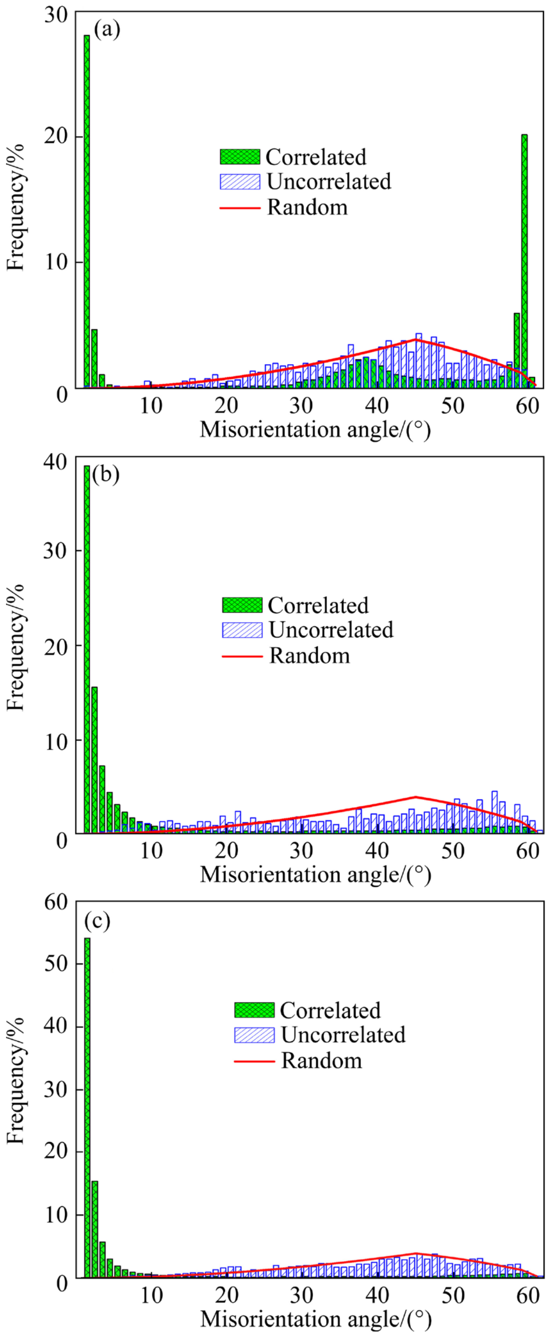

Fig. 14 Distribution of misorientation angles of HAZ$_{\text{J}_\text{H}}$(a), HAZ$_{\text{J}_\text{L}}$ (b) and J$_\text{O}$ (c) samples

Table 3 Fractions of LAGB, MAGB and HAGB

Sample	LAGB	MAGB	HAGB
HAZ$_{\text{J}_\text{H}}$	0.35	0.01	0.64
HAZ$_{\text{J}_\text{L}}$	0.68	0.13	0.19
J$_\text{O}$	0.80	0.07	0.13

Based on Schmid law, if the resolved shear stress (τ) on the slip plane and in the slip direction reaches a certain critical value, the slip system can be activated. The τ in the slip direction can be expressed below [37]:

$$\tau=\frac{F}{A}\cos\lambda\cdot\cos\phi \tag{2}$$

where F is the loading force, A is the section area of sample (F/A is the stress), λ is the angle between stress axis and the slip direction, and ϕ is the angle between stress axis and the normal direction of the slip plane. In Eq. (2), the cos λ·cos ϕ is defined as Schmid factor (SF). Therefore, the SF can be utilized to describe the likelihood of slip system initiation in a specific direction within a crystalline material, indicating that a higher SF corresponds to a greater probability of slip system activation [38,39]. As shown in Fig. 15, as the heat increases, the SF initially increases and then declines. This changing trend is the same as the variation behavior of the deformed grain (Figs. 12 and 15). Accordingly, the HAZ$_{\text{J}_\text{L}}$, with the highest SF value, is more susceptible to slip, indicating that both heat and impact influence the plastic deformation abilities of the samples. However, the HAZ$_{\text{J}_\text{H}}$, with the lowest SF value, may exhibit improved mechanical properties because of recrystallization caused by the heat. Furthermore, since the texture primarily relies on the movement of the slip system during plastic deformation, the SF results correspond to the evolution of texture and deformed grain (Figs. 12, 13 and 15) [40−42].

4 Conclusions

(1) There are deposition layers composed of oxides and compounds of Cu, Al, Zn, and Mg elements on the Cu−Cr−Zr rail sample surfaces after simulated launch, indicating the occurrence of arc ablation. The thickness of these deposition layers increases with the rise in heat, which is associated with the melting and deposition of Al armature on the rail surfaces.

(2) The Brinell hardness of the simulated launch samples is higher than that of the original sample, ascribing to the formation of deposition layer and deformation hardening during the launch process. The corrosion resistance of the simulated launch samples increases with the thickness of the deposition layer. The crystallization temperature range of the samples is related to the composition of the deposition layer, resulting in the varied surface

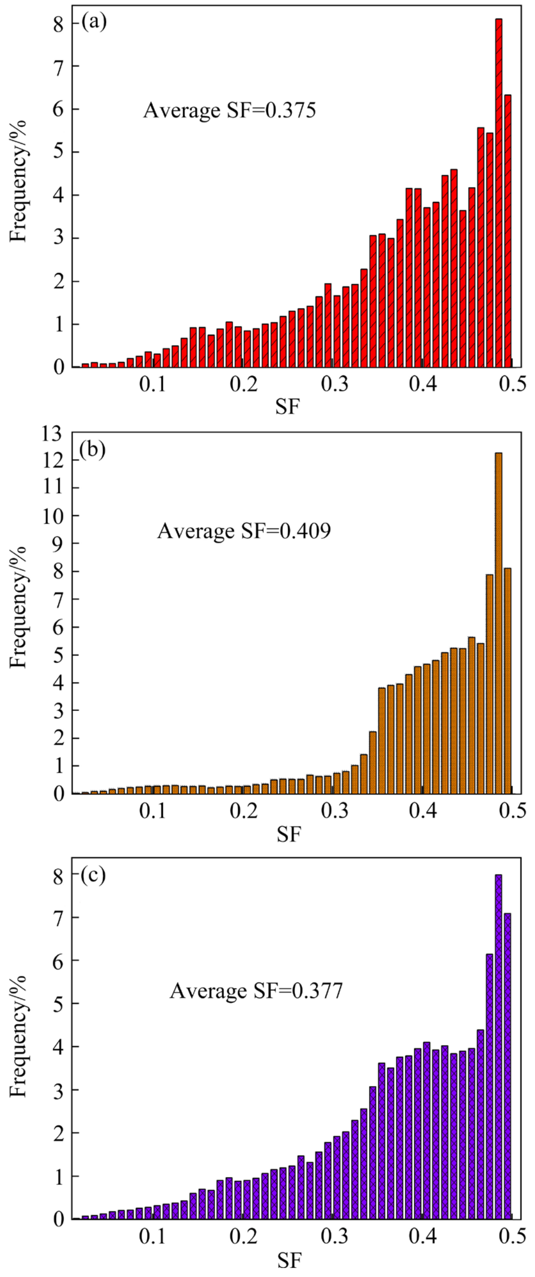

Fig. 15 Distribution of Schmid factors (SF) of samples: (a) HAZ$_{\mathrm{J_H}}$; (b) HAZ$_{\mathrm{J_L}}$; (c) $\mathrm{J_O}$

properties. The heat can influence the recrystallization degree and cause the texture change, while the impact can alter the amount of deformation grains.

(3) The heat and impact play a key role in the structural evolution and performance of electromagnetic railgun rail. Different speed sections of the rail exhibit distinct ablation characteristics and the service performances. Consequently, targeted treatments of different speed sections of the rail can enhance its service life and safety.

CRediT authorship contribution statement

Ke-chang SHEN: Methodology, Investigation, Visualization, Writing – Original draft, Writing − Review & editing; **Qing-tao GONG:** Funding acquisition, Writing – Review & editing; **Zhong-yu SUN:** Supervision; **Hong-tu SUN:** Funding acquisition, Data curation; **Bin-jie MA:** Visualization; **Wei-min WANG**: Conceptualization, Funding acquisition, Writing – Review & editing.

Declaration of competing interest

The authors declare that they have no known competing financial interests or personal relationships that could have appeared to influence the work reported in this paper.

Acknowledgments

This work was financially supported by the Key Research and Development Program of China (No. 2022YFB2404102), the National Natural Science Foundation of China (Nos. 51971093, 52171158, 52101196), the Key Research and Development Program of Shandong Province, China (Nos. 2020ZLYS11, 2021ZLGX01, 2022CXGC020308, 2023CXGC010308), the Major Innovation Projects of Shandong Province, China (Nos. 2020CXGC010701, 2020CXGC010702), the Young Taishan Scholars, China (No. tsqn202211184), the Shandong Provincial Natural Science Foundation, China (No. ZR2022ME137), the Yantai Science and Technology Planning Project, China (No. 2021ZDCX001), and the Open Project Program of Shandong Marine Aerospace Equipment Technological Innovation Center (Ludong University), China (No. MAETIC2021-11).

Supplementary Materials

Supplementary Materials in this paper can be found at: http://tnmsc.csu.edu.cn/download/14-p2589-2023-1125-Supplementary_Materials.pdf.

References

[1] XIE Hong-bin, YANG Hui-ya, YU Jian, GAO Ming-yu, SHOU Jian-dong, FANG You-tong, LIU Jia-bin, WANG Hong-tao. Research progress on advanced rail materials for electromagnetic railgun technology [J]. Defence Technology, 2021, 17(2): 429−439.

[2] LIN Qing-hua, LI Bao-ming. Numerical simulation of dynamic large deformation and fracture damage for solid armature in electromagnetic railgun [J]. Defence Technology, 2020, 16(2): 348−353.

[3] YANG Hai-te, WANG Wen-wei-jiao, WANG Chen, WANG Jian, ZHOU Jian-hui, TONG Chang-qing, CHEN Jun-feng,

WANG Bing-shu. Effects of aging process on properties and precipitation kinetics of Cu−Cr−Zr alloy strips [J]. Transactions of Nonferrous Metals Society of China, 2023, 33(8): 2439−2448.

[4] CALDATTO DALAN F, LIMA ANDREANI G F, TRAVESSA D N, FAIZOV I A, FAIZOVA S, CARDOSO K R. Effect of ECAP processing on distribution of second phase particles, hardness and electrical conductivity of Cu−0.81Cr−0.07Zr alloy [J]. Transactions of Nonferrous Metals Society of China, 2022, 32(1): 217−232.

[5] XIA Cheng-dong, PANG Yong, JIA Yan-lin, NI Cheng-yuan, SHENG Xiao-fei, WANG Su-fen, JIANG Xiao-ying, ZHOU Zhao-zhong. Orientation relationships between precipitates and matrix and their crystallographic transformation in a Cu−Cr−Zr alloy [J]. Materials Science and Engineering A, 2022, 850: 143576.

[6] ZHANG Chao-min, JIANG Yong, ZHOU Yan-jun, GUO Xiu-hua, SONG Ke-xing. First-principles insights into micro-alloying roles of Zr in Cu−Cr−Zr alloys [J]. Journal of Materials Research and Technology, 2023, 24: 824−832.

[7] HAN Jun-qing, WU Yu-ying, ZHAO Kai, LIU Si-da, GAO Tong, LIU Xiang-fa. Effect of boron on aging strengthened phase and properties of Cu−Cr−Zr alloy [J]. Journal of Materials Research and Technology, 2022, 19: 532−541.

[8] WANG Y D, LIU F C, XUE P, ZHANG H, WU L H, NI D R, XIAO B L, MA Z Y. Thermal stability behaviors of ultrafine-grained Cu−Cr−Zr alloy processed by friction stir processing and rolling methods [J]. Journal of Alloys and Compounds, 2023, 950: 169957.

[9] LI Wei-jian, SHAO Wen-zhu, XIE Ning, ZHANG Lu, LI Yuan-ru, YANG Meng-shi, CHEN Bao-an, ZHANG Qiang, WANG Qiang, ZHEN Liang. Air arc erosion behavior of CuZr/Zn_2SnO_4 electrical contact materials [J]. Journal of Alloys and Compounds, 2018, 743: 697−706.

[10] ZHOU Kai, CHEN Wen-ge, FENG Pei, YAN Fang-long, FU Yong-qing. Arc ablation behavior and microstructure evolution of plastically deformed and micro-alloyed Cu−Cr−Zr alloys [J]. Journal of Alloys and Compounds, 2020, 820: 153123.

[11] XIA Sheng-guo, HU Yu-yang, CHEN Li-xue, HE Jun-jia, YUAN Zhao, HE Heng-xin, YAN Ping, LI Jun. Experimental studies on melt erosion at rail-armature contact of rail launcher in current range of 10−20 kA/mm [J]. IEEE Transactions on Plasma Science, 2017, 45(7): 1667−1672.

[12] STEFANI F, MERRILL R. Experiments to measure melt-wave erosion in railgun armatures [J]. IEEE Transactions on Magnetics, 2003, 39(1): 188−192.

[13] MACHADO B I, MURR L E, MARTINEZ E, GAYTAN S M, SATAPATHY S. Materials characterization of railgun erosion phenomena [J]. Materials Science and Engineering A, 2011, 528(25/26): 7552−7559.

[14] LI Jia-zhi, DING Hua, LI Bao-mian, WANG Li. Microstructure evolution and properties of a Cu−Cr−Zr alloy with high strength and high conductivity [J]. Materials Science and Engineering A, 2021, 819: 141464.

[15] YAN Fang-long, CHEN Wen-ge, FENG Pei, DONG Long-long, YANG Tao, REN Shu-xin, FU Yong-qing. Microstructure evolution and enhanced properties of Cu−Cr−Zr alloys through synergistic effects of alloying, heat treatment and low-energy cyclic impact [J]. Journal of Materials Research, 2020, 35(20): 2746−2755.

[16] ZHOU Yu, WU Gao-hui. Materials analysis and testing technology [M]. Harbin: Harbin Institute of Technology Publisher, 2007. (in Chinese)

[17] SHEN Ke-chang, LI Gui-hua, WANG Wei-min. Thermal expansion behavior, microhardness and electrochemical corrosion resistance properties of $Au_{52}Cu_{27}Ag_{17-x}(NiZn_{0.5})_x$ alloys [J]. Transactions of Nonferrous Metals Society of China, 2016, 26(11): 2900−2909.

[18] CAO Zhong-qiu, BIAN Jing, XUE Rong, LIU Wei-hua. Electrochemical corrosion behavior of Cu−40Ni−20Cr alloys with different grain sizes in solutions containing chloride ions [J]. Transactions of Nonferrous Metals Society of China, 2007, 17(6): 1236−1241.

[19] XIAO Zhu, LI Zhou, ZHU An-yin, ZHAO Yu-yuan, CHEN Jing-lin, ZHU Yun-tian. Surface characterization and corrosion behavior of a novel gold-imitation copper alloy with high tarnish resistance in salt spray environment [J]. Corrosion Science, 2013, 76: 42−51.

[20] BAO Wei-zong, XIANG Tao, CHEN Jie, DU Peng, ZHANG Zong-wei, XIE Guo-qiang. Corrosion behavior of high-performance crystalline CuCrZr/amorphous CuZrAl composites in NaCl solution [J]. Journal of Materials Research and Technology, 2022, 21: 5004−5017.

[21] CHENG Yu-lin, FENG Tian, LÜ Jia-hui, HU Pan-feng, CHENG Ying-liang. Plasma electrolytic oxidation behavior and corrosion resistance of brass in aluminate electrolyte containing NaH_2PO_4 or Na_2SiO_3 [J]. Transactions of Nonferrous Metals Society of China, 2022, 32(12): 3985−3997.

[22] WANG Xing, YAO Ping-ping, LI Yu-xing, ZHOU Hai-bing, XIAO Ye-long, DENG Min-wen, KANG Li, ZHOU Pei-yu. Effects of material transfer evolution on tribological behavior in CuCrZr alloy paired with 7075 Al alloy under current-carrying [J]. Tribology International, 2023, 179: 107960.

[23] JIA Zheng-feng, SU Yu-chang, XIA Yan-qiu, SHAO Xin, SONG Yan-xin, NI Jun-jie. Friction and wear behavior of Cu−Cr−Zr alloy lubricated with acid rain [J]. Industrial Lubrication and Tribology, 2014, 66(3): 473−480.

[24] ARBELÁEZ O, REINA T R, IVANOVA S, BUSTAMANTE F, VILLA A L, CENTENO M A, ODRIOZOLA J A. Mono and bimetallic Cu−Ni structured catalysts for the water gas shift reaction [J]. Applied Catalysis A: General, 2015, 497: 1−9.

[25] TSAI C H, CHEN S Y, SONG J M, CHEN I G, LEE H Y. Thermal stability of Cu@Ag core−shell nanoparticles [J]. Corrosion Science, 2013, 74: 123−129.

[26] LI Wei-hua, HU Li-chao, ZHANG Sheng-tao, HOU Bao-rong. Effects of two fungicides on the corrosion resistance of copper in 3.5% NaCl solution under various conditions [J]. Corrosion Science, 2011, 53(2): 735−745.

[27] ZHANG Y N, ZI J L, ZHENG M S, ZHU J W. Corrosion behavior of copper with minor alloying addition in chloride solution [J]. Journal of Alloys and Compounds, 2008, 462(1/2): 240−243.

[28] LI Xiao-xian, WANG Xiang, CHEN Bao-quan, GAO Meng-yan, JIANG Chang, YUAN Hai-xiang, ZHANG Xue-hui, LIANG Tong-xiang. Effect of ultrasonic surface

rolling process on the surface properties of CuCr alloy [J]. Vacuum, 2023, 209: 111819.

[29] HATAKEYAMA M, OKADA K, SUNADA S, SATO K. Effect of dispersion particles and precipitates on the corrosion properties of ODS−Cu, Cu−Cr−Zr and Cu−Cr alloys in Na_2SO_4 solutions [J]. Nuclear Materials and Energy, 2022, 31: 101159.

[30] GHOSH K S, HILAL M, BOSE S. Corrosion behavior of 2024 Al−Cu−Mg alloy of various tempers [J]. Transactions of Nonferrous Metals Society of China, 2013, 23(11): 3215−3227.

[31] LIU Yu-ling, ZHOU Peng, LIU Shu-hong, DU Yong. Experimental investigation and thermodynamic description of the Cu−Cr−Zr system [J]. Calphad, 2017, 59: 1−11.

[32] WANG Jun-feng, CHEN Jin-shui, GUO Cheng-jun, ZHANG Jian-bo, XIAO Xiang-peng, YANG Bin. Effect of heat treatment on low cycle fatigue properties of Cu−Cr−Zr alloy [J]. Materials Characterization, 2019, 158: 109940.

[33] CHEN T A, CHUU C P, TSENG C C, WEN C K, WONG H S P, PAN S Y, LI R T, CHAO T A, CHUEH W C, ZHANG Y F, FU Q, YAKOBSON B I, CHANG W H, LI L J. Wafer-scale single-crystal hexagonal boron nitride monolayers on Cu(111) [J]. Nature, 2020, 579(7798): 219−223.

[34] LI Lin-lin, ZHANG Zhen-jun, ZHANG Peng, ZHANG Zhe-feng. A review on the fatigue cracking of twin boundaries: Crystallographic orientation and stacking fault energy [J]. Progress in Materials Science, 2023, 131: 101011.

[35] CHAI Lin-jiang, LUAN Bai-feng, XIAO Dong-ping, ZHANG Min, MURTY K L, LIU Qing. Microstructural and textural evolution of commercially pure Zr sheet rolled at room and liquid nitrogen temperatures [J]. Materials & Design, 2015, 85: 296−308.

[36] HAN Jing-yu, CHEN Juan, PENG Li-ming, TAN Shuai, WU Yu-juan, ZHENG Fei-yan, YI Hong. Microstructure, texture and mechanical properties of friction stir processed Mg−14Gd alloys [J]. Materials & Design, 2017, 130: 90−102.

[37] XIA Da-biao, CHEN Xiang, HUANG Guang-sheng, JIANG Bin, TANG Ai-tao, YANG Hong, GAVRAS S, HUANG Yuan-ding, HORT N, PAN Fu-sheng. Calculation of Schmid factor in Mg alloys: Influence of stress state [J]. Scripta Materialia, 2019, 171: 31−35.

[38] MILLETT J C F, FENSIN S J, OWEN G D, EFTINK B P, LEAR C, WHITEMAN G, GRAY G T. The mechanical and microstructural response of single crystal aluminium to one dimensional shock loading: The effects of orientation [J]. Acta Materialia, 2023, 246: 118727.

[39] ZHANG Sai-fei, ZENG Wei-dong, ZHAO Qin-yang, GE Li-ling, ZHANG Min. In situ SEM study of tensile deformation of a near-β titanium alloy [J]. Materials Science and Engineering A, 2017, 708: 574−581.

[40] HAN Xiu-zhu, HU Li, JIA Dong-yong, CHEN Jia-ming, ZHOU Tao, JIANG Shu-yong, TIAN Zheng. Role of unusual double-peak texture in significantly enhancing cold rolling formability of AZ31 magnesium alloy sheet [J]. Transactions of Nonferrous Metals Society of China, 2023, 33(8): 2351−2364.

[41] GUO Fei, ZHANG Ding-fei, WU Hua-yi, JIANG Lu-yao, PAN Fu-sheng. The role of Al content on deformation behavior and related texture evolution during hot rolling of Mg−Al−Zn alloys [J]. Journal of Alloys and Compounds, 2017, 695: 396−403.

[42] RAKSHIT R, SARKAR A, PANDA S K, MANDAL S. Influence of out-of-plane stretch forming induced different strain paths on micro-texture evolution, slip system activity and Taylor factor distribution in Al−Li alloy [J]. Materials Science and Engineering A, 2022, 830: 142267.

电磁轨道炮 Cu−Cr−Zr 合金轨道在模拟发射后的损伤特性

神克常[1]，巩庆涛[1]，孙忠玉[1]，孙宏图[1]，马彬洁[1]，王伟民[2]

1. 鲁东大学 蔚山船舶与海洋学院，烟台 264025；
2. 山东大学 材料科学与工程学院 材料液固结构演变与加工教育部重点实验室，济南 250061

摘　要：研究模拟发射后不同速度段 Cu−Cr−Zr 合金轨道的损伤特性。采用 XRD、XPS、EBSD、SEM、硬度测试、电化学测试和 DSC 等手段对合金样品的显微组织、形貌和性能进行研究。研究发现，在模拟发射样品表面形成了沉积层。沉积层的厚度和表面粗糙度随着热效应的增加而增加，表明电弧烧蚀损伤程度与发射速度的相关性。样品的硬度变化归因于沉积层和变形硬化的影响。表面沉积层影响样品的耐腐蚀性和结晶特性，从而导致后续服役性能发生变化。此外，样品的表面织构和塑性变形能力与再结晶程度和变形晶粒数量有关。

关键词：Cu−Cr−Zr 合金；电磁轨道炮；电弧烧蚀；显微组织；性能

(Edited by Wei-ping CHEN)